Revision 2

Elastic properties and structures of pyrope glass under high pressures

Word Count: 6624 words

NAOKI HISANO[1], TATSUYA SAKAMAKI[1*], TOMONORI OHASHI[1], KEN-ICHI FUNAKOSHI[2], YUJI HIGO[3], YUKI SHIBAZAKI[4], AND AKIO SUZUKI[1]

[1]Department of Earth Science, Graduate School of Science, Tohoku University, Sendai, Miyagi 980-8578, Japan.

[2]Neutron Science & Technology Center, Comprehensive Research Organization for Science and Society (CROSS), Tokai, Ibaraki 319-1106, Japan.

[3]Japan Synchrotron Radiation Research Institute, Sayo, Hyogo 679-5198, Japan.

[4]National Institute for Materials Science, Tsukuba, Ibaraki 305-0044, Japan.

Corresponding author:

Tatsuya Sakamaki

Department of Earth Science, Tohoku University, Sendai 980-8578, Japan

TEL: +81-22-795-6666

FAX: +81-22-795-6666

E-mail: sakamaki@tohoku.ac.jp

This is the peer-reviewed, final accepted version for American Mineralogist, published by the Mineralogical Society of America.
The published version is subject to change. Cite as Authors (Year) Title. American Mineralogist, in press.
DOI: https://doi.org/10.2138/am-2020-7410. http://www.minsocam.org/

ABSTRACT

X-ray diffraction analysis and ultrasonic measurements of glass with a pyrope composition were conducted to determine its structural and elastic properties at pressures ranging from 1 atm to 12.9 GPa. Our results indicated that the structural evolution in the glass was closely related to changes in the compression wave velocity (V_P), the shear wave velocity (V_S), and the Poisson ratio. We observed three modes of pyrope glass compression. Moderate shrinkage in the intermediate-range ordered structure occurred at pressures below 6 GPa. Significant shrinkage in the intermediate-range ordering was observed at pressures between 6 GPa and 9 GPa. We observed changes in the short-range ordered structure at pressures above 9 GPa, which were associated with an increase in the coordination number of tetrahedral cations. The absolute values of V_P and V_S in pyrope glass were similar to those in magnesium-bearing silicate glasses with enstatite and diopside compositions. However, the velocities were higher than those observed in sodium aluminum silicate glasses with jadeite and albite compositions. This indicated that the absolute values were governed by the initial density of the glass, which was determined by its chemical composition. In terms of pressure, the velocity minimum in pyrope glass was observed at ~5 GPa, which was similar to the velocity minima in fully polymerized glasses, such as jadeite and albite. The degree of polymerization in the pyrope glass was intermediate, and it had a relatively polymerized network. A drastic increase in velocity was observed when the pyrope glass was subjected to pressures above 7–8 GPa, and the velocity exceeded that observed in silicate glasses. Densification phenomenon, such as an increase in the

Al coordination number, was efficiently promoted. This was because the cationic field strength of Mg^{2+} exceeded that of typical non-network forming cations. Magnesium cations may have an important role in controlling the behavior of silicate glass, and partially melted mantle becomes enriched with Mg under pressure. Studying Mg-bearing aluminosilicate glasses can thus help us to better understand the behavior of magma deep in the interior of the Earth.

Keywords: Pyrope glass; elastic wave velocity; structure; high pressure

Introduction

The atomic structures of magmas are closely related to their physical, chemical, and thermal properties (Mysen et al. 1982; 1985; Kushiro and Mysen 2002). Examining silicate glasses can provide insight into magma structure. Many analytical methods have been used to investigate pressure-induced structural and physical changes in silicate (SiO_2) glasses. These include Raman spectroscopy (McMillan et al. 1984; Devine and Arndt 1987), X-ray diffraction analysis (Meade et al. 1992; Inamura et al. 2004; Sato and Funamori 2010), neutron diffraction analysis (Inamura et al. 2001), molecular dynamics simulation (Jin et al. 1994; Trachenko and Dove 2002, 2003), Brillouin scattering analysis (Zha et al. 1994; Murakami and Bass 2010), and ultrasonic techniques (Yokoyama et al. 2010; Kono et al. 2012). A large increase in density of glasses is attributed to a significant shrinkage of the intermediate-range order (IRO) network, which is indicated by a drastic change in the first sharp diffraction peak (FSDP) in the structure factor, $S(Q)$ (Susman et al. 1991; Inamura et al. 2001; Trachenko and Dove 2002).

Aluminum is one of the most abundant elements on Earth, and it significantly influences

the properties of silicate networks in melts and glasses. Al^{3+} is an intermediate species in silicate melts, meaning that it can be incorporated into a network modified depending on the composition (Riebling 1966; Mysen et al. 1981). In fully polymerized melts, such as jadeite and albite, all of the TO_4 tetrahedra (T = Si^{4+}, Al^{3+}) are linked by shared oxygen anions and form a three-dimensional network structure. Alkali metal ions, such as Na^+ and K^+, and alkali earth metal ions, including Mg^{2+} and Ca^{2+}, can also affect the behavior of melts. These cations are known as network modifiers, and they can break the Si–O–Si bonds that join adjacent SiO_4 tetrahedra (Mysen et al. 1982).

An increase in the coordination number (CN), or the number of coordinated oxygen atoms around a network-forming metal, leads to densification during pressure-induced structural evolution. Nuclear magnetic resonance (NMR) spectroscopy studies of aluminosilicate glasses have shown that the Al–O CN increases at lower pressures than the Si–O CN (Stebbins and Sykes 1990; Yarger et al. 1995; Lee et al. 2004; Allwardt et al. 2007). Based on the results of these NMR studies, an increase in the Al–O CN is affected by the field strengths of cationic modifiers. The cationic field strength is equal to the charge of the cation divided by the square of the distance between the cation and an oxygen atom (Allwardt et al. 2005, 2007; Kelsey et al. 2009). In other words, modifiers with high cationic field strengths promote increases in the Al–O CN. The cationic field strengths of alkali and alkali earth metal cations follow the order K < Na < Ca < Mg, which means that Mg-aluminosilicate glasses can undergo structural changes at relatively low pressures (McMillan and Kirkpatrick 1992; Toplis et al. 2000; Neuville et al. 2008).

Pyrope ($Mg_3Al_2Si_3O_{12}$) is a Mg-aluminosilicate mineral that is abundant in the Earth's upper mantle. A change in the slope of the pyrope melting curve from approximately 7 GPa to 10

GPa suggests that pressure induces a change in aluminum coordination (Irifune and Ohtani 1986; Zhang and Herzberg 1994). The structures and elasticity of Mg-aluminosilicate glasses have been investigated extensively via neutron and X-ray diffraction analysis (Guignard and Cormier, 2008) and NMR spectroscopy (McMillan and Kirkpatrick, 1992; Toplis et al. 2000; Neuville et al. 2008). Those of pyrope glasses have been studied at ambient pressure via XRD analysis (Okuno and Marumo 1997) and NMR spectroscopy (Lee et al. 2016). However, the properties of pyrope at high pressures are poorly understood.

In this study, we investigated the elastic wave velocities in pyrope glass at pressures ranging up to 12.9 GPa using a pulse-echo overlap ultrasonic technique to better understand the dependence of its elastic properties on pressure. Information about the structure of the glass at pressures up to 12.9 GPa was obtained by performing multi-angle energy-dispersive X-ray diffraction analysis. Herein we describe pressure-induced changes in the wave velocity in pyrope glass and its structure, and we discuss the relationship between its elastic properties and structural evolution.

Experimental Methods

Reagent grade SiO_2, MgO, and Al_2O_3 were mixed to obtain a pyrope composition ($Mg_3Al_2Si_3O_{12}$) in an agate mortar with acetone for 1 h. The mixed powder was melted at 1,873 K and quenched to ambient temperature to form the glass. In glass with a pyrope composition, the ratio of non-bridging oxygen (NBO) anions to tetrahedrally coordinated cations (T), or NBO/T, is 0.8 (Mysen et al. 1982). The NBO/T ratio in a silicate network is a fundamental indicator of its degree of polymerization. A fully polymerized network has an NBO/T ratio of 0, while a TO_4 monomer assembly has an NBO/T ratio of 4. Based on the NBO/T ratio of pyrope

glass (0.8), it has a relatively polymerized structure.

For our structural investigations, we performed energy-dispersive X-ray diffraction analysis at pressures ranging from 1 atm to 12.9 GPa using the PF-AR NE5C beamline at the High Energy Accelerator Research Organization (KEK) Facility in Tsukuba, Japan. We used a MAX80 cubic multi-anvil apparatus (Shimomura et al. 1984) in combination with MA6-6 assembly (Nishiyama et al. 2008) to generate high pressures. The incident X-ray beam was collimated by directing it through two sets of 0.1 mm vertical slits and 0.2 mm horizontal slits. The diffracted beam was collimated by placing a 0.1 mm gap collimator 43 mm downstream from the sample and two receiving slits 40 mm downstream from the scattering slits. A 0.2 mm vertical receiving slit and either a 0.3 mm ($2\theta \leq 8°$) or 1.0 mm ($2\theta \geq 11°$) horizontal receiving slit were used. A Ge solid-state detector (Ge-SSD) with a 2048 multichannel analyzer was mounted on a two theta arm, which enabled us to accurately control the diffraction angle. Diffraction patterns were collected at fixed diffraction angles (2θ) of 3°, 4°, 5°, 6°, 8°, 11°, 14°, 17°, 21°, 25°, and 30°. Collection times varied and depended on the diffraction angle, since the intensity decreased as 2θ increased. Pattern collection continued until the maximum intensity reached at least 7,000 counts. An example of diffraction patterns of pyrope glass is shown in Figure 1. The connection of multiple data sets collected at various 2θ angles was conducted to minimize the differences between intensity patterns in each overlap region. This procedure has been performed based on the Monte Carlo simulation method (MCEDX) developed by Funakoshi (1997). This method enables us to obtain the reliable intensity profile without using any theoretical functions. The structure factor, $S(Q)$, was obtained from the X-ray diffraction data using the MCEDX analytical program. $S(Q)$ is given by Equation (1).

This is the peer-reviewed, final accepted version for American Mineralogist, published by the Mineralogical Society of America.
The published version is subject to change. Cite as Authors (Year) Title. American Mineralogist, in press.
DOI: https://doi.org/10.2138/am-2020-7410. http://www.minsocam.org/

$$S(Q) = \left\{ I^{\mathrm{coh}}(Q)/N - \sum_i c_i [f_i(Q)]^2 \right\} \Big/ \left[\sum_i c_i f_i(Q) \right]^2 + 1, \quad (1)$$

where N is the number of atoms and $I^{\mathrm{coh}}(Q)$ is the coherent intensity due to atomic correlation. c_i and $f_i(Q)$ are the concentration and the atomic scattering factor of the i^{th} atom, respectively. The summation is taken over the atomic species. Q is the magnitude of the scattering vector given by Equation (2).

$$Q = \frac{4\pi E \sin\theta}{hc} = \frac{4\pi \sin\theta}{\lambda}, \quad (2)$$

where λ is the X-ray wavelength, E is the X-ray energy, θ is half of the diffraction angle, h is Planck's constant, and c is the speed of light in a vacuum. The local structure in real space is given by the pair distribution function, $g(r)$ (Kaplow et al. 1965), which is the Fourier transform of $S(Q)$ according to Equation (3).

$$g(r) = 1 + \frac{1}{2\pi^2 nr} \int_{Q_{\min}}^{Q_{\max}} Q[S(Q) - 1] \sin(Qr) \mathrm{d}r, \quad (3)$$

where n is the number density, and r is the radial distance.

Ultrasonic experiments to measure elastic wave velocities were conducted at pressures of up to 12.9 GPa using a SPEED-1500 Kawai multi-anvil apparatus installed on the BL04B1 beamline at SPring-8 (Utsumi et al. 1998). Cobalt-doped magnesia was used as the pressure medium. The sample was sandwiched between fully densified alumina cylinders, which served as a buffer rod and back-reflector. The top and bottom surfaces of the glass sample, the alumina buffer rod, and the back-reflector were polished with diamond paste (1 μm) to ensure good mechanical contact. Two pieces of gold foil were placed on the top and bottom of the sample as markers for length measurements. Radiographs were collected using a CCD camera to determine the length of the sample under high pressures. The pressures were determined using the NaCl

equation of state (Decker 1971). The scattered X-rays were detected using a Ge SSD paired with a 4096 multichannel analyzer. High-pressure elastic wave velocity measurements were performed using the ultrasonic pulse-echo overlap method. A 10° rotated Y-cut $LiNbO_3$ transducer was used as the ultrasonic signal generator and receiver. The signals were recorded at a sampling rate of 1×10^{10} points per second. Detailed descriptions of the ultrasonic measurements can be found in Higo et al. (2008, 2009, 2018). An example of X-ray radiography image and ultrasonic signal is shown in Figure 2. At an ultrasonic wave frequency of 42 MHz, the accuracy of the travel time is not less than one tenth of the period, ~2.4 ns (Higo et al. 2009). An uncertainty of ±2.4 ns in the travel time generated uncertainties of no more than ±0.95% and ±0.68% in the compression and shear wave velocities, respectively. An uncertainty of <1 pixel in the sample length was a conservative estimate, because the positions of the sample interfaces with the buffer rod and back-reflector were determined with a standard deviation of <1.8 pixel. An uncertainty of ±1.8 pixel in the sample length corresponded to an error of ±0.31% in measurements of both compression and shear wave velocity. We concluded that the overall uncertainties in the compression and shear wave velocity measurements were less than 1.00% and ±0.74%, respectively.

Results and Discussion

Structure of pyrope glass under pressure

The structure of pyrope glass was analyzed at pressures ranging from 1 atm to 12.9 GPa. The structure factor obtained at each pressure is shown in Fig. 3. For silicates, the FSDP is typically centered at 2–3 $Å^{-1}$ in the $S(Q)$. This is indicated by the solid arrow in Fig. 3. The FSDP is generally a signature of the …–T–O–T–… IRO structure in a silicate network (Elliott

1991). The FSDP positions of various silicate glasses under pressure are shown in Fig. 4. The FSDP position under ambient conditions is associated with the void volume in the network structure (e.g., Onodera et al. 2019) of the glass, which is mainly governed by its chemical composition. Pure silica glass has the spongiest network, while sodium aluminosilicates (albite, jadeite) have smaller void volumes. The void volume in magnesium aluminosilicate (pyrope) glass is smaller still, and calcium magnesium silicate (diopside) glasses have the lowest void volumes. In other words, the relationship between pressure and the FSDP position is governed by the combination of metal cations in the silicate glass. The FSDP position of pyrope glass at ambient pressure is between those of albite/jadeite glass and diopside glass. In terms of the dependence of the FSDP position on pressure, a shift in the peak to a higher Q indicates pressure-induced shrinkage of the IRO structure in real space. This corresponds to a change in the network TO_4 configuration, such as a decrease in the tetrahedral T–O–T bond angle and a reduction in the void volume in the network. The FSDP positions of pyrope and depolymerized glasses are less sensitive to pressure than those of fully depolymerized glass. Wang et al. (2014) investigated the dichotomy between pressure and the FSDP position using structural data from both X-ray diffraction and molecular dynamics analyses of the jadeite-diopside join. They observed an interesting phenomenon in a fully polymerized jadeite melt. The number of bridging oxygen (BO) atoms monotonically decreased with increasing pressure. This indicated that the fully polymerized melt had a spongy structure. Since every oxygen anion was a BO, the initial response to pressure was a decrease in the T–O–T bond angle, which resulted in bond breakage in the continuous network. The first stage of compression thus involved a pressure-induced decrease in the BO population, i.e. depolymerization. In contrast, an increase in the BO population and a monotonic decrease in the NBO population were observed in the

depolymerized diopside melt. Due to the reduced connectivity of its TO_4 network, the depolymerized diopside melt had a much weaker structure that could rearrange without breaking many BO bonds. A rapid decrease in the NBO population with pressure caused the structure to polymerize. Similar behavior has been observed in depolymerized $MgO\text{-}SiO_2$ glasses under pressure (Wilding et al. 2012).

Since the network in pyrope glass is moderately polymerized (NBO/T = 0.8), the FSDP position of pyrope glass is affected less by pressure than those of fully polymerized glasses. A monotonic shift in the FSDP toward higher Q values was observed as the pressure increased up to 7.1 GPa (Fig. 4), which suggested continuous shrinkage of the IRO network structure. The FSDP position underwent a relatively large shift to higher Q values at pressures between 7.1 GPa and 8.8 GPa, and the shift continued monotonically up to 12.9 GPa.

The local structure in the glass was determined from the pair distribution function, $g(r)$, which was obtained by performing a Fourier transformation of $S(Q)$ (Eq. 3). Variations in the $g(r)$ of the pyrope glass with pressure are shown in Fig. 5. The peak near 1.6–1.7 Å corresponded to T–O, or the length of the bonds between tetrahedrally coordinated cations and oxygen anions in the pyrope glass. The Mg^{2+}/Al^{3+} molar ratio in pyrope glass is 1.5. All of the Al cations in the glass are incorporated into the network, while interstitial Mg cations balance the charge. The shoulder peaks in the ranges of 2.0–2.2 Å and 2.6–2.8 Å represented the Mg–O and O–O bond distances, respectively. The positions of these peaks were consistent with those reported by Okuno and Marumo (1993) at ambient pressure. The peak observed near 1.6–1.7 Å did not have any distinctive features that would enable us to distinguish between Si–O and Al–O bonds, so it was taken as the average of the Si–O and Al–O bond distances. It is important to determine the T–O bond length to understand the properties of the TO_4 tetrahedra, which are the basic units of

225 silicate glass. The T–O bond length in pyrope glass is shown as a function of pressure in Fig. 6.
226 The Si–O and Al–O bond lengths in crystalline pyrope (Zhang et al. 1998) are plotted for
227 comparison. The length of T–O bonds in pyrope glass remained stable up to 11.6 GPa, then
228 increased. The T–O peak broadened near 12.9 GPa. This implied that the average CN of
229 tetrahedrally coordinated cations increased near 13 GPa. In contrast, the Si–O and Al–O bond
230 lengths in crystalline pyrope slightly decreased with pressure.

231 Al is much more susceptible to changes in coordination than Si (Waff 1975; Yarger et al.
232 1995; Lee et al. 2004). The fraction of highly coordinated Al (i.e. $^{[5,6]}$Al) in ternary
233 aluminosilicate glasses also increases as the cationic field strengths of network-modifying
234 cations increase (Neuville et al. 2008; Kelsey et al. 2008; Ifterkhar et al. 2012; Jaworski et al.
235 2012), and the cationic field strength of Mg^{2+} is higher than that of Na^{+}, K^{+}, and Ca^{2+} (McMillan
236 and Kirkpatrick 1992; Toplis et al. 2000; Neuville et al. 2008).

237 The T–T bond length near 3.1 Å provided information about the relationship between
238 adjacent TO_4 tetrahedra, which was important for understanding the three-dimensional (3D)
239 nature of the glass structure. The calculated average T–O–T bond angles were based on the
240 relationship between the T–O and T–T bond lengths. The T–O–T angle was set equal to
241 2arcsin{[T–T]/2[T–O]} assuming that corner-sharing TO_4 tetrahedra formed a 3D framework
242 structure. The dependence of the T–O bond length, the T–T bond length, and the T–O–T angle in
243 pyrope glass on pressure is illustrated in Fig. 7. The T–T bond length was more sensitive to
244 pressure than that of T–O. Broadening of the T–T peaks above 7.1 GPa could have been due to
245 topological disordering. The dependence of the T–O–T angle on pressure followed a similar
246 trend to that observed in the T–T bond length. The T–O–T angle decreased by 6.9% from 141.4°
247 at 1 atm to 131.7° at 12.9 GPa. The T–O–T angle was closely related to the IRO network

structure, and a decrease in the T–O–T angle indicated a transition to a more compact structure. This compression may have been related to an increase in the proportion of edge-sharing TO_4 tetrahedra relative to corner-sharing TO_4 tetrahedra.

Crystalline pyrope has a cubic structure with Si and Al CNs of 4 and 6, respectively (Novak and Gibbs 1971). SiO_4 tetrahedra and AlO_6 octahedra share corners to form the 3D network. Cavities within the network structure can be viewed as distorted cubes comprised of eight oxygen atoms surrounding a Mg cation. Therefore, oxygen is bonded to one Si, one Al, and two Mg. The Si–O–Al angle in crystalline pyrope decreases from 131.0° at ambient pressure to 128.8° at 11.53 GPa (Zhang et al. 1998). This decrease was far less pronounced than the changes in the T–O–T angle in pyrope glass observed in this pressure range. The structure of pyrope glass differs significantly from that of crystalline pyrope in terms of Al coordination. Lee et al. (2016) investigated the environment around Al in pyrope glass at ambient pressure via NMR spectroscopy. Most of the Al in pyrope glass has a CN of 4, and the amount of $^{[5,6]}$Al ranges from ~7% to 10%. In other words, the CN of Al in pyrope glass differs from the CN of Al in crystalline pyrope.

Elastic wave velocities in pyrope glass under pressure

The experimental elastic wave velocity measurements are summarized in Table 1. The dependencies of the compression wave velocity (V_P) and shear wave velocity (V_S) on pressure are illustrated in Figs. 8 and 9, respectively. The velocities in silica (Zha et al. 1994), jadeite, albite, diopside (Sakamaki et al. 2014), and enstatite glasses (Sanchez-Valle and Bass 2010) are plotted for comparison. The velocities at ambient pressure were governed by the chemical

composition, particularly the Mg content. According to Birch's law, there is a linear relationship between density and velocity at a constant mean atomic weight (Birch 1961). This means that the velocities in magnesium-bearing silicate glasses are much higher than those in less dense, magnesium-free glasses.

Marked changes in the elastic wave velocities in pyrope glass were observed in three pressure regions. At pressures below 6 GPa, the slopes of the elastic wave velocities were negative. At pressures between 6 GPa and 9 GPa, the velocities increased sharply with pressure. At pressures above 9 GPa, increases in the velocities were moderate. In terms of composition, the impact of pressure on velocity was either the appearance of a velocity minimum or the absence of a minimum. These results indicated that the degree of polymerization fundamentally affected the behavior of compressed silicate glass. In polymerized glasses, both the V_P and V_S initially decreased with pressure, then increased above a threshold pressure. Softening was much more pronounced in the V_S than the V_P. This can be seen in Figs. 8 and 9. In contrast, the V_P and V_S in depolymerized glasses, such as diopside and enstatite glasses, changed only slightly as the pressure increased. This behavior differed from that observed in the polymerized glasses. The marked differences between the impacts of pressure on the elastic wave velocities suggested that the dominant structural changes in the glasses in each compressed region differed significantly.

The Poisson ratio of pyrope glass

The Poisson ratio (σ) is shown as a function of pressure in Fig. 10. The Poisson ratio is obtained directly from the measured elastic wave velocities by Equation (4).

This is the peer-reviewed, final accepted version for American Mineralogist, published by the Mineralogical Society of America.
The published version is subject to change. Cite as Authors (Year) Title. American Mineralogist, in press.
DOI: https://doi.org/10.2138/am-2020-7410. http://www.minsocam.org/

$$\sigma = \frac{V_P^2 - 2V_S^2}{2(V_P^2 - V_S^2)}. \quad (4)$$

The Poisson ratio in depolymerized glasses is close to 0.3 at ambient pressure and seems to increase monotonically (Sakamaki et al. 2014). The Poisson ratio in fully polymerized glasses is ~0.2 under ambient conditions, although it increases rapidly with pressure (Sakamaki et al. 2014). The dependence of the Poisson ratio in pyrope glass on pressure was similar to that observed in depolymerized glasses. Although the error is large, there may be an anomalous behavior at pressures between 6 GPa and 9 GPa. A dramatic drop in the Poisson ratio indicated that the volume of the glass decreased significantly.

Compression behavior of pyrope glass

Based on our structural measurements, we identified three pressure regions in which structural changes were induced. Moderate structural changes characterized by a monotonous shift in the FSDP position to higher Q values were observed at pressures at or below ~6 GPa. The dependence of the FSDP position in $S(Q)$ on pressure changed at pressures between 6 and 9 GPa, and the T–T bond length and T–O–T angle in $g(r)$ both decreased. At pressures at or above 9 GPa, the T–O bond length increased. In the lower pressure range from 1 atm to ~6 GPa, there was an inverse relationship between the elastic wave velocity in the pyrope glass and pressure. Moderate shrinkage of the IRO structure was observed, while the short-range structure was less sensitive to pressure. Non-elastic deformation dominated the first stage of compaction. In the mid-pressure range (6–9 GPa), shrinkage of the IRO structure in the pyrope glass was fairly significant. The dependence of the elastic properties on pressure became positive. The structure of the glass became more compact due to topological rearrangement associated with a decrease

in the T–O–T angle. A change in the compaction mechanism may have been related to changes in the pyrope melting curve near 7 GPa (Irifune and Ohtani 1986; Zhang and Herzberg 1994). In the high-pressure range (≥9 GPa), pressure-induced changes in the elastic properties of the pyrope glass and the FSDP position were moderate. First-principles molecular dynamics simulations have revealed a relationship between the structure of anorthite ($CaAl_2Si_2O_8$) glass and the velocity of sound waves (Ghosh and Karki 2018). Based on the results of that study, the tetrahedral cations underwent primarily topological changes. These did not significantly affect the average bond distance or coordination during the initial stages of cold compression (0–10 GPa). The velocity of sound waves began to increase sharply at pressures above ~10 GPa, and the T–O bond length increased. Similar changes in velocity and structure have been observed in SiO_2 glass at pressures in the range of 15–20 GPa (Zha et al. 1994; Benmore et al. 2010). A structural analysis of SiO_2 glass also indicated that the dependence of the Si–O bond length on pressure changed from negative to positive, and the Si–O CN increased at the same pressures (Benmore et al. 2010). The relationship between sound wave velocity and the T–O bond length may be a common feature in silicate glasses, although the changes occur at different pressures due to variations in chemical composition. The onset of such increases is particularly affected by the presence or absence of aluminum.

Implications

In this study, we demonstrated that the structural densification of pyrope glass was closely related to changes in its elastic properties. The compression behavior of pyrope glass was distinctly different in three pressure regions. Moderate shrinkage of the IRO was observed at pressures below GPa. IRO shrinkage was relatively pronounced at pressures in the range from 6

GPa to 9 GPa. The T–O CN increased at pressures above 9 GPa. Compared to other silicate glasses, the chemical composition of pyrope glass had a more significant effect on its properties and pressure dependence (Figs. 6–8). Although pyrope, diopside, and enstatite were all magnesium-bearing silicate glasses with velocities that had similar absolute values at low experimental pressures, the velocity in pyrope glass was highest at higher pressures. This was due to densification related to the presence of Al. Magnesium is abundant in the partially melted regions of the Earth's mantle, particularly in the deeper regions (Nakajima et al. 2019). Al-bearing hydrous minerals are stable in the lower mantle (Xu and Inoue 2019). Hydrous minerals have an important role in mantle melting, because they become sources of H_2O in the lower mantle when they are dehydrated. Partial melts that form in the deep mantle are rich in magnesium and aluminum, which are incorporated into the melt. Therefore, knowledge about magnesium-bearing aluminosilicate glass can further our understanding of deep magma behavior.

Acknowledgments

This research was performed with the support of JSPS KAKENHI Grants JP15H05828, JP17H04860, and JP17K18797. Ultrasonic experiments were performed at the BL04B1 of Spring-8 with the approval of the Japan Synchrotron Radiation Research Institute (JASRI) (Proposal Nos. 2016B1111, 2017A1384, 2017B1267, 2017B1270, 2018A1302, and 2018B1180). X-ray diffraction experiments were conducted on the AR-NE5C beamline with the approval of the KEK (Proposal Nos. 2014G524 and 2017G580).

References

Allwardt, J.R., Stebbins, J.F., Schmidt, B.C., Frost, D.J., Withers, A.C., and Hirschmann, M.M.

(2005) Aluminum coordination and the densification of high-pressure aluminosilicate glasses. American Mineralogist, 90, 1218–1222.

Allwardt, J.R., Stebbins, J.F., Terasaki, H., Du, L.S., Frost, D.J., Withers, A.C., Hirschmann, M.M., Suzuki, A., and Ohtani, E. (2007) Effect of structural transitions on properties of high-pressure silicate melts: ^{27}Al NMR, glass densities, and melt viscosities. American Mineralogist, 92, 1093–1104.

Benmore, C.J., Soignard, E., Amin, A., Guthrie, M., Shastri, S.D., Lee, P.L., and Yarger, J.L. (2010) Structural and topological changes in silica glass at pressure. Physical Review B, 81, 054105.

Birch, F. (1961) The velocity of compressional waves in rocks to 10 kilobars, part 2. Journal of Geophysical Research, 66, 2199–2224.

Decker, D.L. (1971) High-pressure equation of state for NaCl, KCl, and CsCl. Journal of Applied Physics. 42, 3239–3244.

Devine, R.A.B., and Arndt, J. (1987) Si-O bond-length modification in pressure-densified amorphous SiO_2. Physical Review B, 35, 9376–9379.

Elliott, S.R. (1991) Medium-range structure order in covalent amorphous solids, Nature, 354, 445–452.

Funakoshi, K. (1997) Energy-dispersive x-ray diffraction for alkali silicate melts using synchrotron radiation under high pressure and temperature. Ph.D. dissertation. Tokyo Institute of Technology.

Ghosh, D.B., Karki, B.B., and Stixrude, L. (2014) First-principles molecular dynamics simulations of $MgSiO_3$ glass: Structure, density, and elasticity at high pressure. American Mineralogist, 99, 1304–1314.

Ghosh, D.B., and Karki, B.B. (2018) First-principles molecular dynamics simulations of anorthite ($CaAl_2Si_2O_8$) glass at high pressure. Physics and Chemistry of Minerals, 45, 575–587.

Guignard, M., and Cormier, L. (2008) Environments of Mg and Al in MgO-Al_2O_3-SiO_2 glasses: A study coupling neutron and X-ray diffraction and Reverse Monte Carlo modeling. Chemical Geology, 256, 111–118.

Higo,Y., Inoue, T., Irifune, T., Funakoshi, K., and Li, B. (2008) Elastic wave velocities of $(Mg_{0.91}Fe_{0.09})_2SiO_4$ ringwoodite under *P*-*T* conditions of the mantle transition region. Physics of the Earth and Planetary Interiors, 166, 167–174.

Higo, Y., Kono, Y., Inoue, T., Irifune, and T., Funakoshi, K. (2009) A system for measuring elastic wave velocity under high pressure and high temperature using a combination of ultrasonic measurement and the multi-anvil apparatus at SPring-8. Journal of Synchrotron Radiation, 16, 762–768.

Higo, Y., Irifune, T., and Funakoshi, K. (2018) Simultaneous high-pressure high-temperature elastic velocity measurement system up to 27 GPa and 1873 K using ultrasonic and synchrotron X-ray techniques. Review of Scientific Instruments, 89, 014501.

Inamura, Y., Arai, M., Nakamura, M., Otomo, T., Kitamura, N., Bennington, S.M., Hannon, and A.C., Buchenau, U. (2001) Intermediate range structure and low-energy dynamics of densified vitreous silica. Journal of Non-Crystalline, Solids, 293–295, 389–393.

Inamura, Y., Katayama, Y., Utsumi, W., and Funakoshi, K. (2004) Transformations in the intermediate-range structure of SiO_2 glass under high pressure and temperature. Physical Review Letters, 93, 011501.

Irifune, T., and Ohtani, E. (1986) Melting of pyrope $Mg_3Al_2Si_3O_{12}$ up to 10 GPa: Possibility of a

pressure-induced structural change in pyrope melt. Journal of Geophysical Research, 91, 9357–9366.

Jin, W., Kalia, R.K., Vashishya P., and Rino, J.P. (1994) Structural transformation in densified silica glass: A molecular-dynamics study. Physical Review B, 50, 118–131.

Kaplow, R., Strong, S.L., and Averbach, B.L. (1965) Radial density functions for liquid mercury and lead. Physical Review, 138, A1336–A1345.

Kelsey, K.E., Stebbins, J.F., Singer D.M., Brown, G.E., Mosenfelder, J.L., and Asimow, P.D. (2009) Cation field strength effects on high pressure aluminosilicate glass structure: Multinuclear NMR and La XAFS results. Geochimica et Cosmochimica Acta, 73, 3914–3933.

Kono, Y., Park, C., Sakamaki, T., Kenny-Benson, C., Shen, G., and Wang, Y. (2012) Simultaneous structure and elastic wave velocity measurement of SiO_2 glass at high pressures and high temperatures in a Paris–Edinburgh cell. Review of Scientific Instruments, 83, 033905.

Kushiro, I., and Mysen, B.O. (2002) A possible effect of melt structure on the Mg-Fe^{2+} partitioning between olivine and melt. Geochimica et Cosmochimica Acta, 66, 2267–2272.

Lee, S.K., Cody, G.D., Fei, Y., and Mysen, B.O. (2004) Nature of polymerization and properties of silicate melts and glasses at high pressure. Geochimica et Cosmochimica Acta, 68, 4189–4200.

Lee, S.K., Kim, H.I., Kim, E.J., Mun, K.Y., and Ryu, S. (2016) Extent of disorder in magnesium aluminosilicate glasses: Insights from ^{27}Al and ^{17}O NMR. The Journal of Physical Chemistry C, 120, 737–749.

Lee, S.K., Lin, J.-F., Cai, Y.Q., Hiraoka, N., Eng, P.J., Okuchi, T., Mao, H.-k., Meng, Y., Hu,

M.Y., Chow, P., Shu, J., Li, B., Fukui, H., Lee, B.H., Kim, H.N., and Yoo, C.-S. (2008) X-ray Raman scattering study of $MgSiO_3$ glass at high pressure: Implication for triclustered $MgSiO_3$ melt in Earth's mantle. Proceedings of the National Academy of Sciences of the United States of America, 105, 7925–7929.

McMillan, P.F., and Kirkpatrick, R.J. (1992) Al coordination in magnesium aluminosilicate glasses. American Mineralogist, 77, 898–900.

McMillan, P., Piriou, B., and Couty, R. (1984) A Raman study of pressure-densified vitreous silica. Journal of Chemical Physics, 81, 4234–4236.

Meade, C., Hemley, R.J., and Mao, H.K. (1992) High-pressure x-ray diffraction of SiO_2 glass. Physical Review Letters, 69, 1387–1390.

Murakami, M., and Bass, J.D. (2010) Spectroscopic evidence for ultrahigh-pressure polymorphism in SiO_2 glass. Physical Review Letters, 104, 025504.

Mysen, B.O., Virgo, and D., Kushiro, I. (1981) The structure role of aluminum in silicate melts – a Raman spectroscopic study at 1 atmosphere. American Mineralogist, 66, 678–701.

Mysen, B.O., Virgo, D., and Seifert, F.A. (1982) The structure of silicate melts : Implications for chemical and physical properties of natural magma. Review of Geophysics and Space Physics, 20. 353–383.

Mysen, B.O., Virgo, D., and Seifert, F.A. (1985) Relationships between properties and structure of aluminosilicate melts. American Mineralogist, 70, 88–105.

Nakajima, A., Sakamaki, T., Kawazoe, T., and Suzuki, A. (2019) Hydrous magnesium-rich magma genesis at the top of the lower mantle. Scientific Reports, 9, 7420.

Neuville, D.R., Cormier, L., Montouillout, V., Florian, P., Millot, F., Rifflet, J-C., and Massiot, D. (2008) Structure of Mg- and Mg/Ca aluminosilicate glasses: ^{27}Al NMR and Raman

spectroscopy investigations. American Mineralogist, 93, 1721–1731.

Nishiyama, N., Wang, Y., Sanehira, T., Irifune, T., and Rivers, M. (2008) Development of the Multi-anvil Assembly 6-6 for DIA and D-DIA type high-pressure apparatuses. High Pressure Research, 28, 307–314.

Novak, G.A., and Gibbs, G.V. (1971) The crystal chemistry of the silicate garnets. American Mineralogist, 56, 791–825.

Okuno, M., and Marumo, F. (1993) The structure analyses of pyrope ($Mg_3Al_2Si_3O_{12}$) and grossular ($Ca_3Al_2Si_3O_{12}$) glasses by X-ray diffraction method. Mineralogical Journal, 16, 407–415.

Onodera, Y., Kohara, S., Tahara, S., Masuno, A., Inoue, H., Shiga, M., Hirata, A., Tsuchiya, K., Hiraoka, Y., Obayashi, I., and others (2019) Understanding diffraction patterns of glassy, liquid and amorphous materials via persistent homology analyses. Journal of the Ceramic Society of Japan, 127, 853–863.

Riebling, E.F. (1966) Structure of sodium aluminosilicate melts containing at least 50 mole% SiO_2 at 1500°C. Journal of Chemical Physics, 44, 2857–2865.

Sakamaki, T., Kono, Y., Wang, Y., Park, C., Yu, T., Jing, Z., and Shen, G. (2014) Contrasting sound velocity and intermediate-range structural order between polymerized and depolymerized silicate glasses under pressure. Earth and Planetary Science Letters, 391, 288–295.

Sanchez-Valle, C., and Bass, J.D. (2010) Elastic and pressure-induced structural changes in vitreous $MgSiO_3$-enstatite to lower mantle pressures. Earth and Planetary Science Letters, 295, 523–530.

Sato, T., and Funamori, N. (2010) High-pressure structural transformation of SiO_2 glass up to

100 GPa. Physical Review B, 82, 184102.

Shim, S.-H., Catalli, K. (2009) Compositional dependence of structural transition pressures in amorphous phases with mantle-related compositions. Earth and Planetary Science Letters, 283, 174–180.

Shimomura, O., Yamaoka, S., Yagi, T., Wakatsuki, M., Tsuji, K., Fukunaga, O., Kawamura, H., Aoki, K., and Akimoto, S. (1984) Multi-anvil type X-ray apparatus for synchrotron radiation. In Materials Research Society Symposia Proceedings Vol. 22, pp. 17–20. Elsevier Science Publishing Company, New York.

Stebbins, J.F., and Sykes, D. (1990) The structure of $NaAlSi_3O_8$ liquid at high pressure: New constraints from NMR spectroscopy. American Mineralogist, 75, 943–946.

Susman, S., Volin, K.J., Montague, D.G., and Price, D.L. (1991) Temperature dependence of the first sharp diffraction peak in vitreous silica. Physical Review B, 43, 11076–11081.

Toplis, M.J., Kohn, S.C., Smith, M.E., and Poplett, I.J.F. (2000) Fivefold-coordinated aluminum in tectosilicate glasses observed by triple quantum MAS NMR. American Mineralogist, 85, 1556–1560.

Trachenko, K., and Dove, M.T. (2002) Densification of silica glass under pressure. Journal of Physics: Condensed Matter, 14, 7449–7459.

Trachenko, K., and Dove, M.T. (2003) Intermediate state in pressurized silica glass: Reversibility window analogue. Physical Review B, 67, 212203.

Utsumi, W., Funakoshi, K., Urakawa, S., Yamakata, M., Tsuji, K., Konishi, H., and Shimomura, O. (1998) SPring-8 beamlines for high pressure science with multi-anvil apparatus. Review of High Pressure Science and Technology, 7, 1484–1486.

Waff, H.S. (1975) Pressure-induced coordination changes in magmatic liquids. Geophysical

499 Research Letters, 2, 193-196.

500 Xu, C., and Inoue, T. (2019) Melting of Al-rich Phase D up to the uppermost lower mantle and
501 transportation of H_2O to the deep Earth. Geochemistry, Geophysics, Geosystems, 20,
502 4382–4389.

503 Yarger, J.L., Smith, K.H., Nieman, R.A., Diefenbacher, J., Wolf, G.H., Poe, B.T., and McMillan,
504 P.F. (1995) Al coordination change in high-pressure aluminosilicate liquids. Science, 270,
505 1964–1967.

506 Yokoyama, A., Matsui, M., Higo, Y., Kono, Y., Irifune, T., and Funakoshi, K. (2010) Elastic
507 wave velocities of silica glass at high temperatures and high pressures .Journal of Applied
508 Physics, 107, 123530.

509 Zha, C.K., Hemley, R.J., Mao, H.K., Duffy, T.S., and Meade, C. (1994) Acoustic velocities and
510 refractive index of SiO_2 glass to 57.5 GPa by Brillouin scattering. Physical Review B, 50,
511 105–112.

512 Zhang, I., Ahsbahs, H., and Kutoglu, A. (1998) Hydrostatic compression and crystal structure of
513 pyrope to 33 GPa. Physics and Chemistry of Minerals, 25, 301–307.

514 Zhang, J., and Herzberg, C. (1994) Melting of pyrope, $Mg_3Al_2Si_3O_{12}$, at 7-16 GPa. American
515 Mineralogist, 79, 497–503.

516

517 **Figure captions**

518 Figure 1. An example of data set collected at 12 .9 GPa.

519 Figure 2. An example of X-ray radiography image of sample (a) and ultrasonic signal (b) at 12.9
520 GPa.

521 Figure 3. Changes in the structure factor ($S(Q)$) of pyrope glass with pressure. The solid arrow
522 indicates the position of the FSDP.

523 Figure 4. FSDP positions of silicate glasses as a function of pressure. The data for silica glass
524 were obtained from Inamura et al. (2004). Values for jadeite, albite, and diopside glasses were
525 obtained from Sakamaki et al. (2014). The error bars are smaller than the symbols.

526 Figure 5. Pair distribution function, $g(r)$, of pyrope glass with pressure.

527 Figure 6. T–O bond length in pyrope glass as a function pressure. The Si–O and Al–O bond
528 lengths in crystalline pyrope are plotted for comparison. The error bars are smaller than the
529 symbols.

530 Figure 7. Dependence of the T–O and T–T bond lengths and the T–O–T angle in pyrope glass on
531 pressure.

532 Figure 8. Compressional wave velocities in silicate glasses as a function of pressure. Data for the
533 silica glass were obtained from Zha et al. (1994). Data for enstatite glass were obtained from
534 Sanchez-Valle and Bass (2010). Values for jadeite, albite, and diopside glasses were obtained
535 from Sakamaki et al. (2014).

536 Figure 9. Shear wave velocities in silicate glasses as a function of pressure. Data for silica glass
537 were obtained from Zha et al. (1994). Values for enstatite glass were obtained from Sanchez-
538 Valle and Bass (2010). Values for jadeite, albite, and diopside glasses were obtained from
539 Sakamaki et al. (2014).

Figure 10. The Poisson ratios of silicate glasses as a function of pressure. Data for silica glass was obtained from Zha et al. (1994). Information for enstatite glass was obtained from Sanchez-Valle and Bass (2010). Values for jadeite, albite, and diopside glasses were obtained from Sakamaki et al. (2014).

Tables

Table 1 Results of sound velocity measurements

Pressure [GPa]	V_P [km/s]	V_S [km/s]	Poisson ratio
2.48(3)	7.06(5)	3.81(2)	0.294(13)
3.01(5)	7.02(5)	3.80(2)	0.293(13)
3.75(6)	6.98(5)	3.76(2)	0.296(12)
4.03(4)	6.95(5)	3.73(2)	0.298(12)
4.62(6)	6.91(5)	3.69(2)	0.300(12)
5.13(7)	6.89(5)	3.67(2)	0.301(13)
5.61(7)	6.88(5)	3.66(2)	0.302(13)
6.11(7)	6.92(5)	3.66(2)	0.305(13)
6.57(5)	7.07(5)	3.72(2)	0.309(13)
7.08(7)	7.11(5)	3.77(2)	0.304(13)
7.55(6)	7.11(5)	3.91(2)	0.283(14)
8.07(2)	7.47(6)	3.96(2)	0.304(14)
8.87(3)	7.79(7)	4.05(3)	0.315(15)
9.93(7)	7.86(7)	4.12(3)	0.310(16)
10.92(7)	7.96(7)	4.18(3)	0.310(16)
12.05(6)	8.16(8)	4.24(3)	0.315(17)
12.85(8)	8.24(8)	4.27(3)	0.317(17)

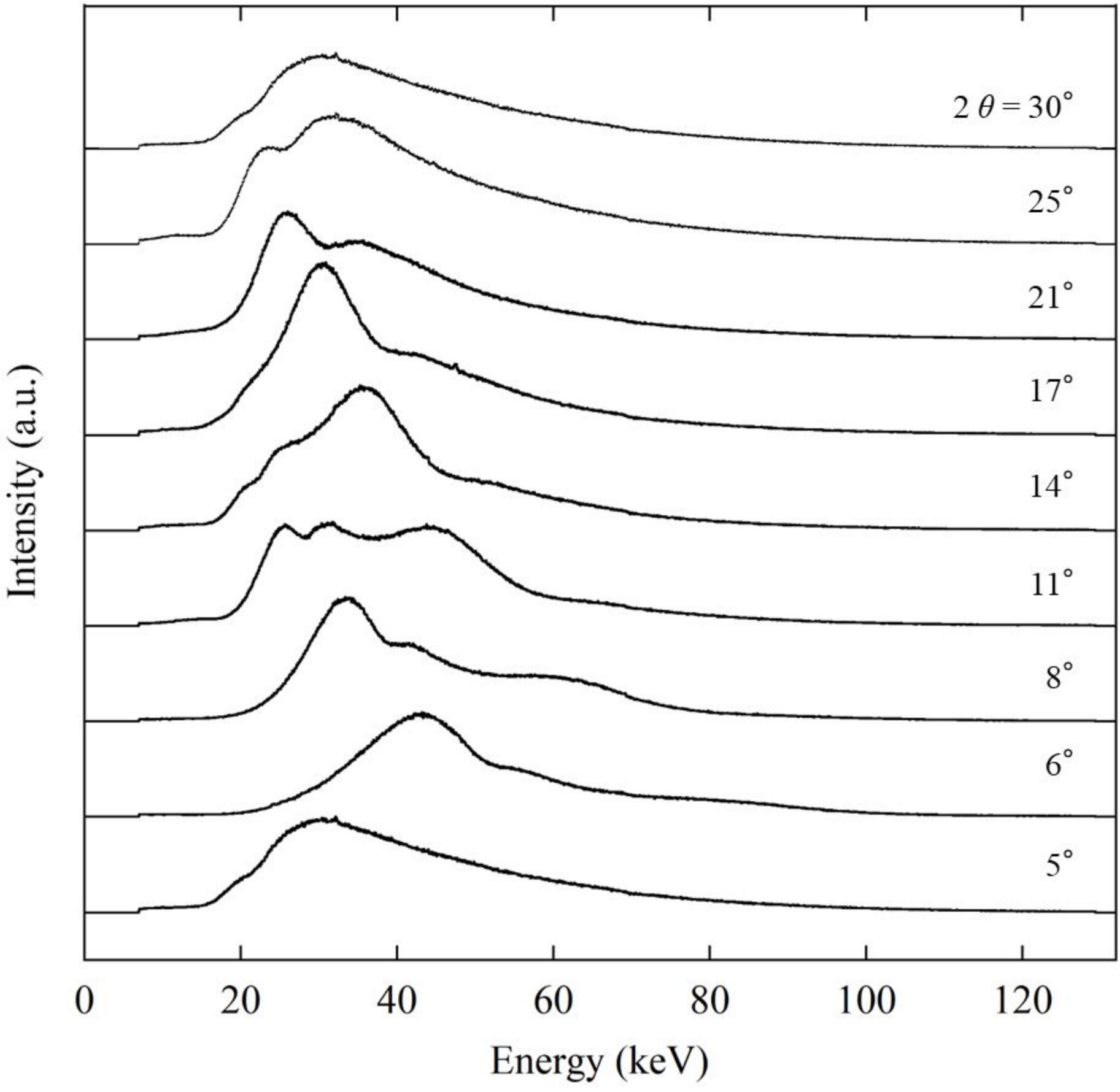
2 θ = 30°
25°
21°
17°
14°
11°
8°
6°
5°
Intensity (a.u.)
0
20
40
60
80
100
120
Energy (keV)

(a)

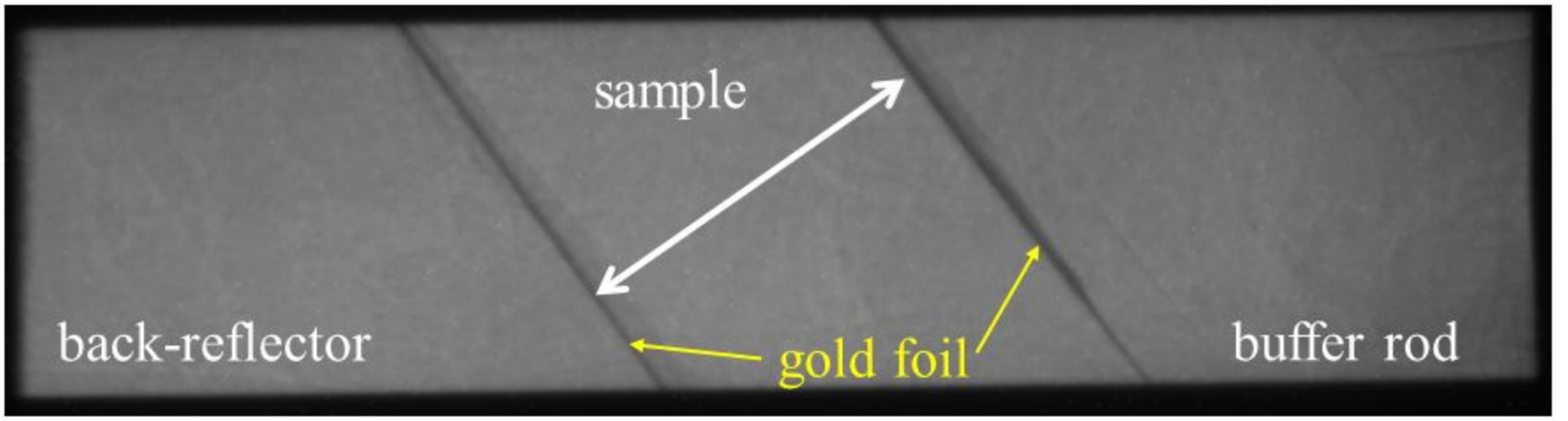
sample
back-reflector
gold foil
buffer rod

(b)

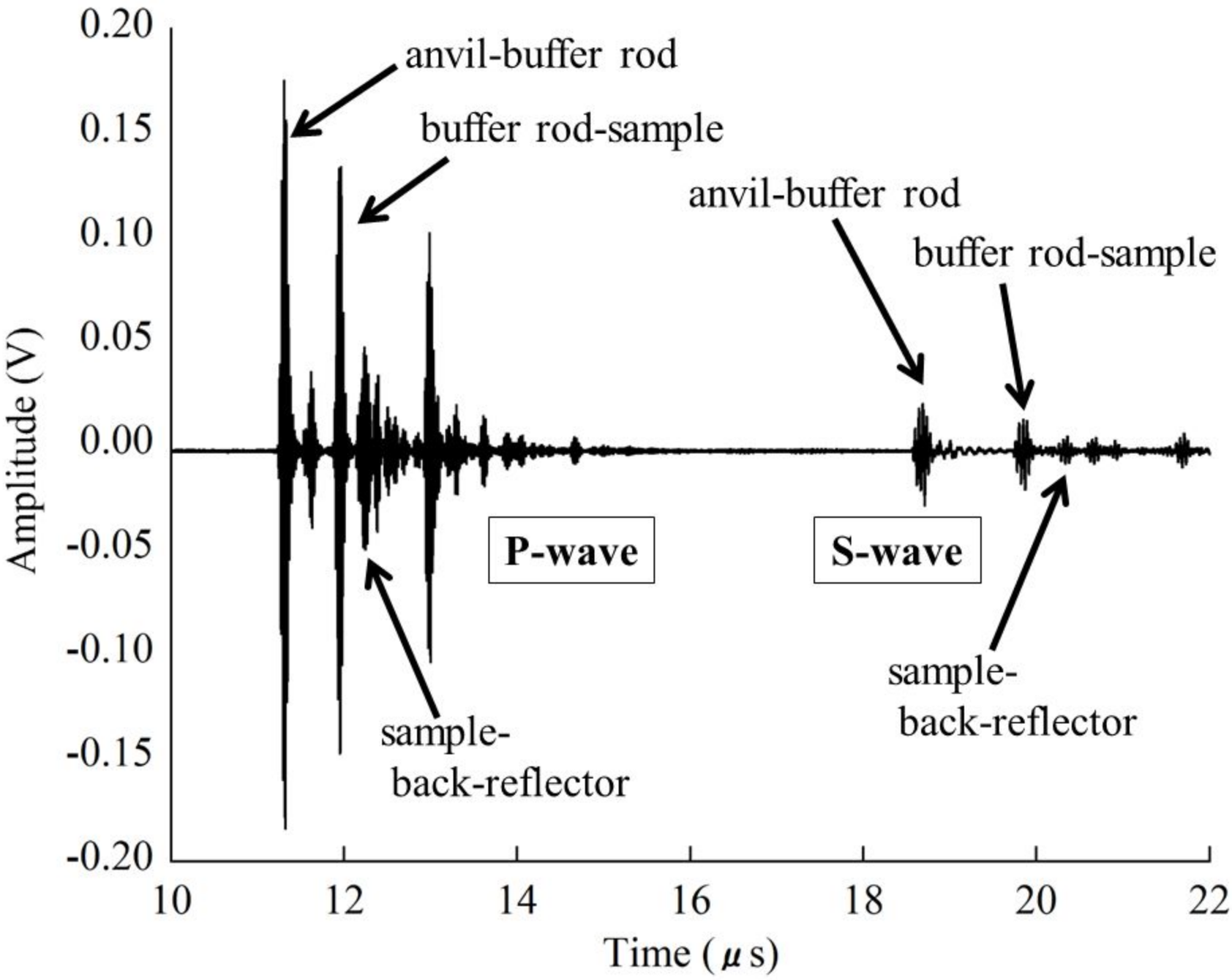
0.20
0.15
0.10
0.05
0.00
-0.05
-0.10
-0.15
-0.20
Amplitude (V)
anvil-buffer rod
buffer rod-sample
anvil-buffer rod
buffer rod-sample
P-wave
S-wave
sample-
back-reflector
sample-
back-reflector
10
12
14
16
18
20
22
Time (μs)

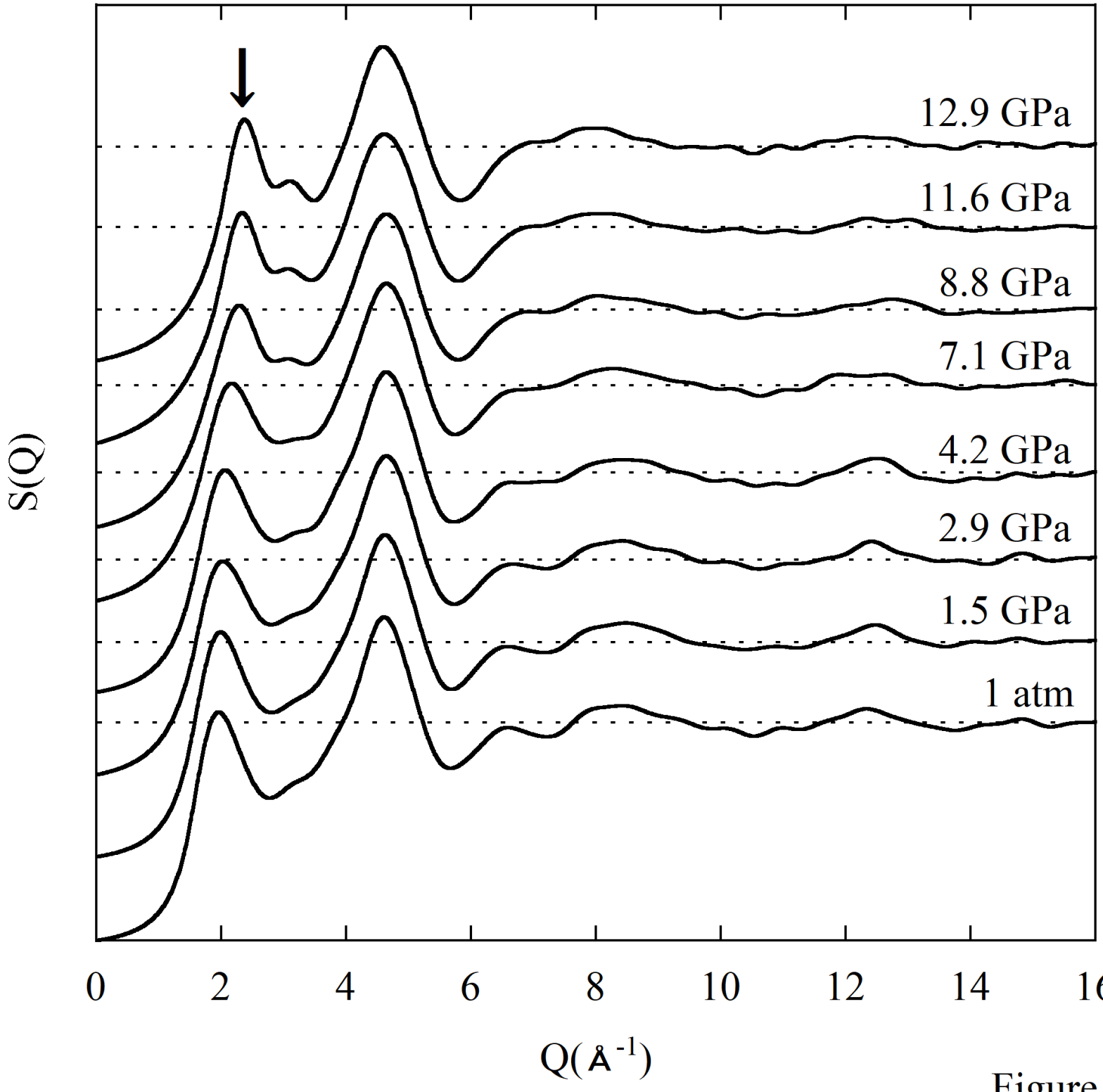
12.9 GPa
11.6 GPa
8.8 GPa
7.1 GPa
4.2 GPa
2.9 GPa
1.5 GPa
1 atm
S(Q)
0
2
4
6
8
10
12
14
16
Q(Å-1)

Figure 1

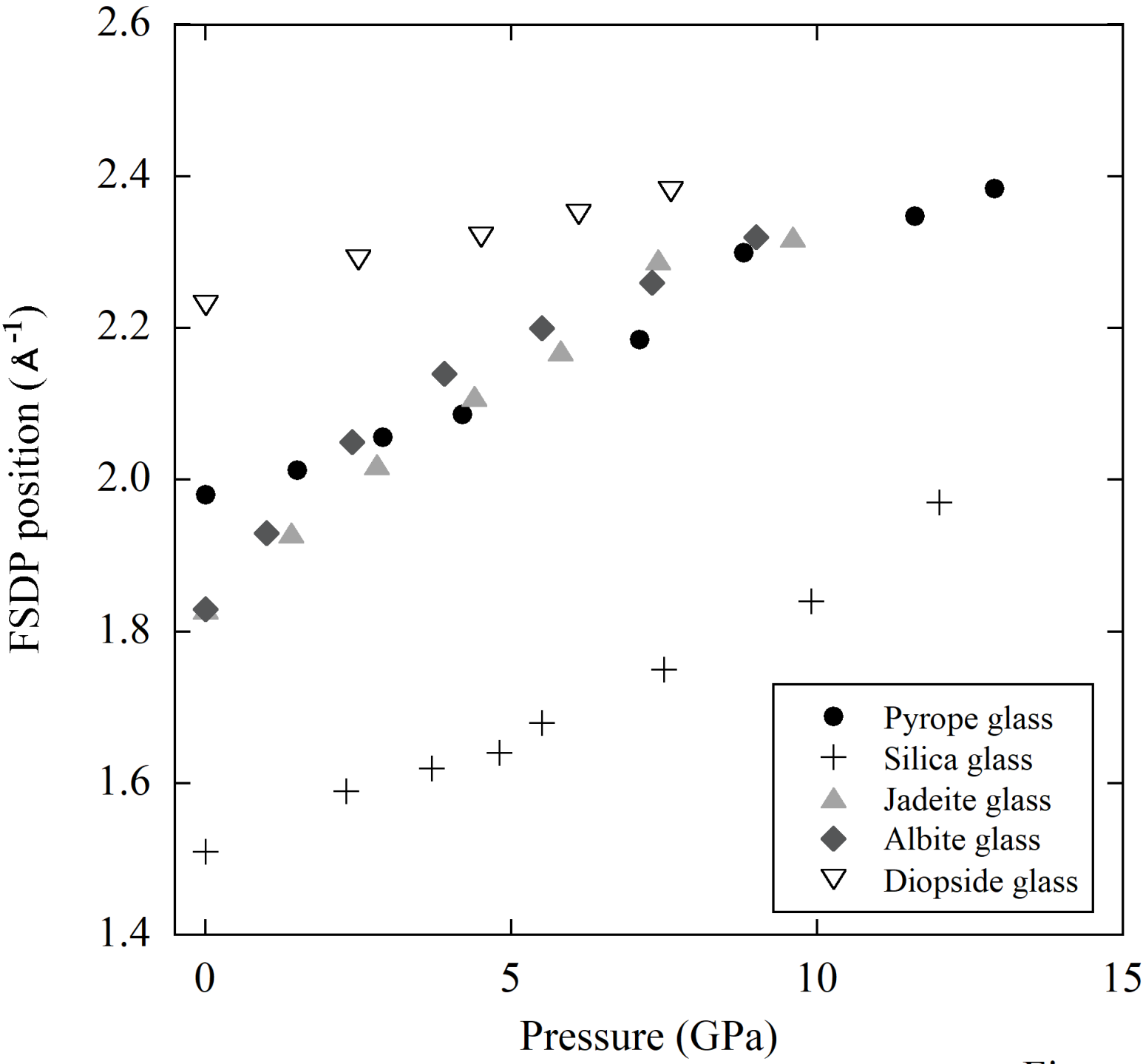
2.6
2.4
2.2
2.0
1.8
1.6
1.4
FSDP position (Å-1)
0
5
10
15
Pressure (GPa)
Pyrope glass
Silica glass
Jadeite glass
Albite glass
Diopside glass

Figure 2

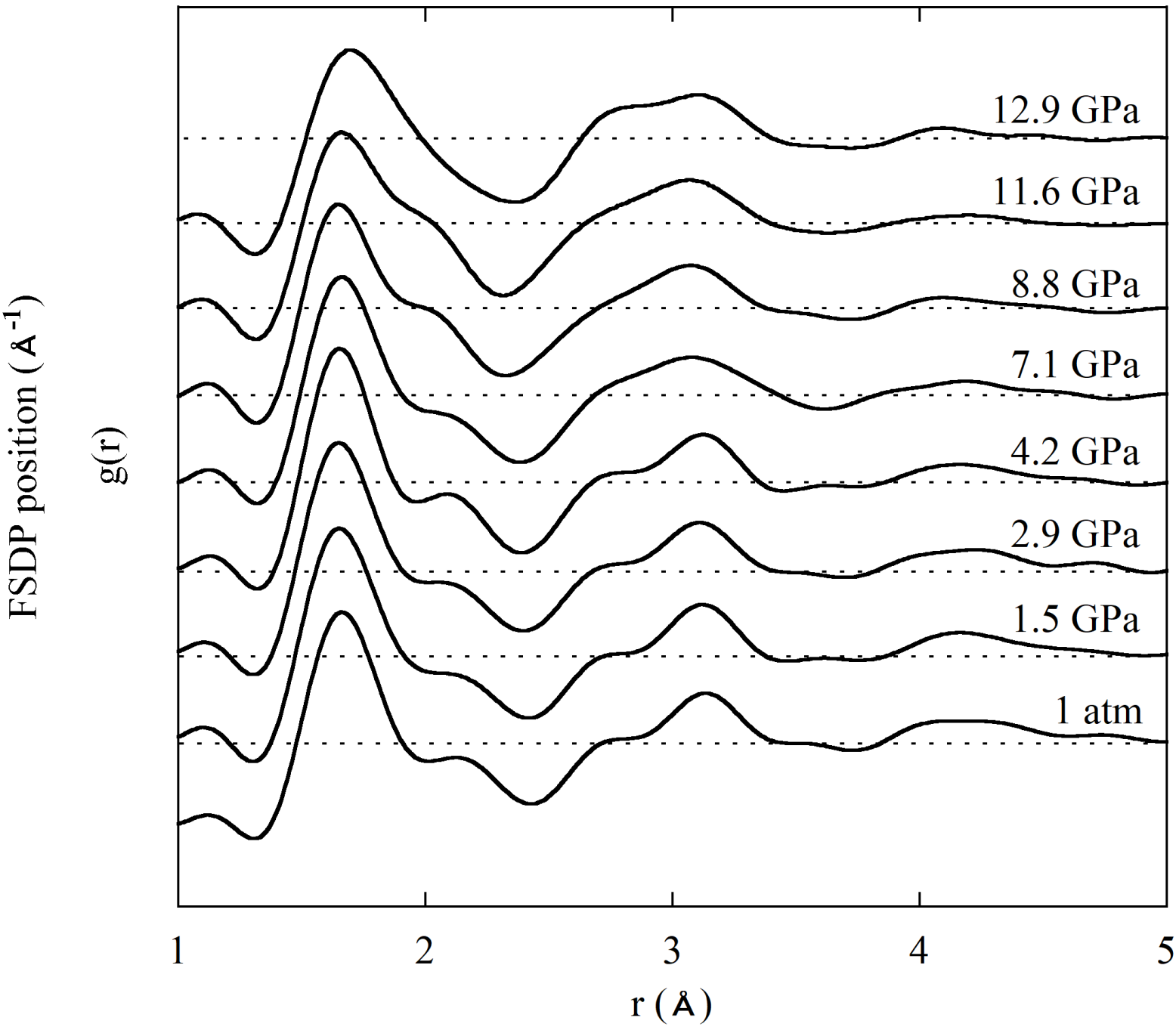
12.9 GPa
11.6 GPa
8.8 GPa
7.1 GPa
4.2 GPa
2.9 GPa
1.5 GPa
1 atm
g(r)
FSDP position (Å -1)
1
2
3
4
5
r (Å)

Figure 3

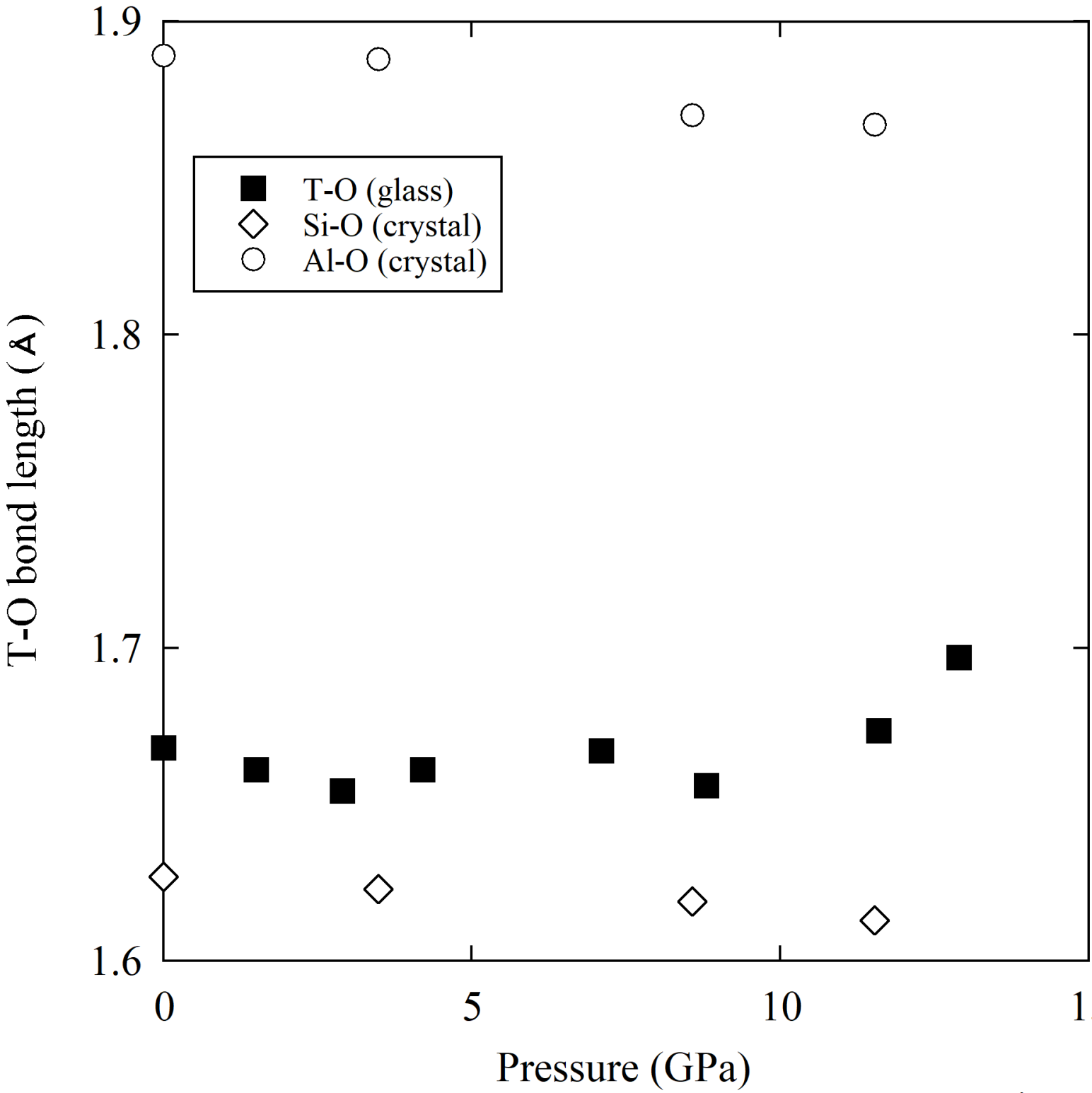
1.9
1.8
1.7
1.6
T-O bond length (Å)
T-O (glass)
Si-O (crystal)
Al-O (crystal)
0
5
10
15
Pressure (GPa)

Figure 4

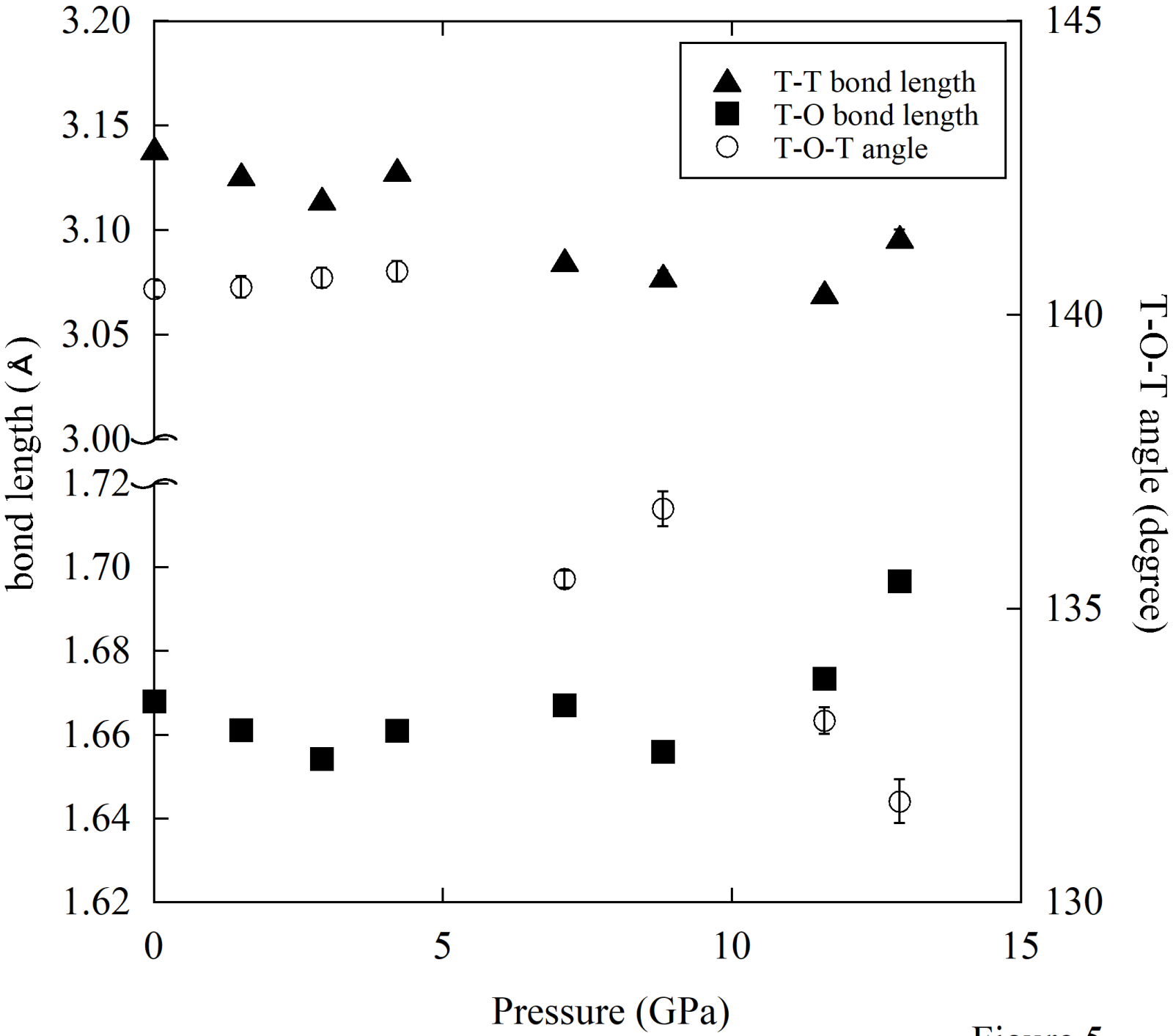
3.20
3.15
3.10
3.05
3.00
1.72
1.70
1.68
1.66
1.64
1.62
bond length (Å)
145
140
135
130
T-O-T angle (degree)
0
5
10
15
Pressure (GPa)
T-T bond length
T-O bond length
T-O-T angle

Figure 5

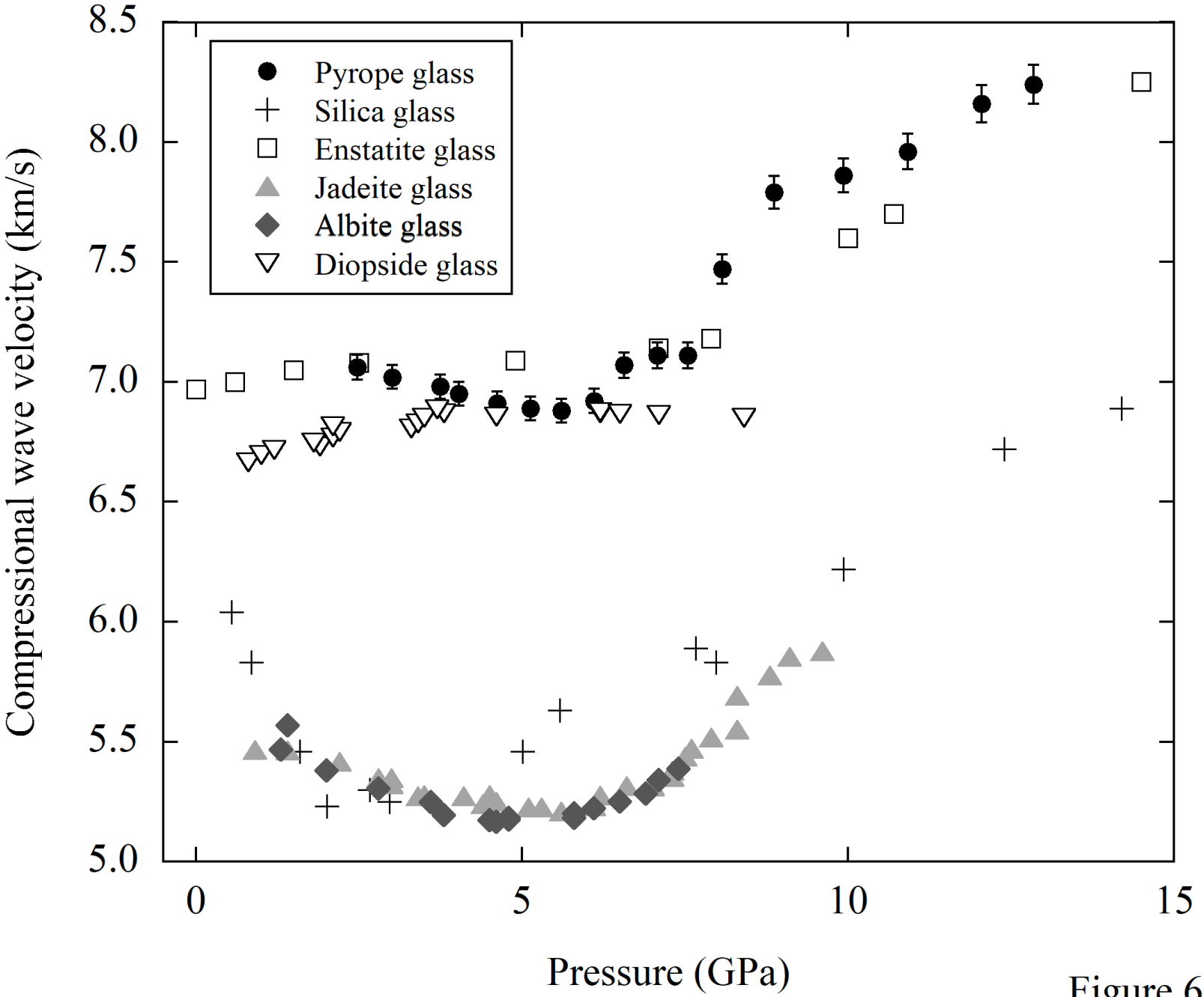
Pyrope glass
Silica glass
Enstatite glass
Jadeite glass
Albite glass
Diopside glass
Compressional wave velocity (km/s)
8.5
8.0
7.5
7.0
6.5
6.0
5.5
5.0
0
5
10
15
Pressure (GPa)

Figure 6

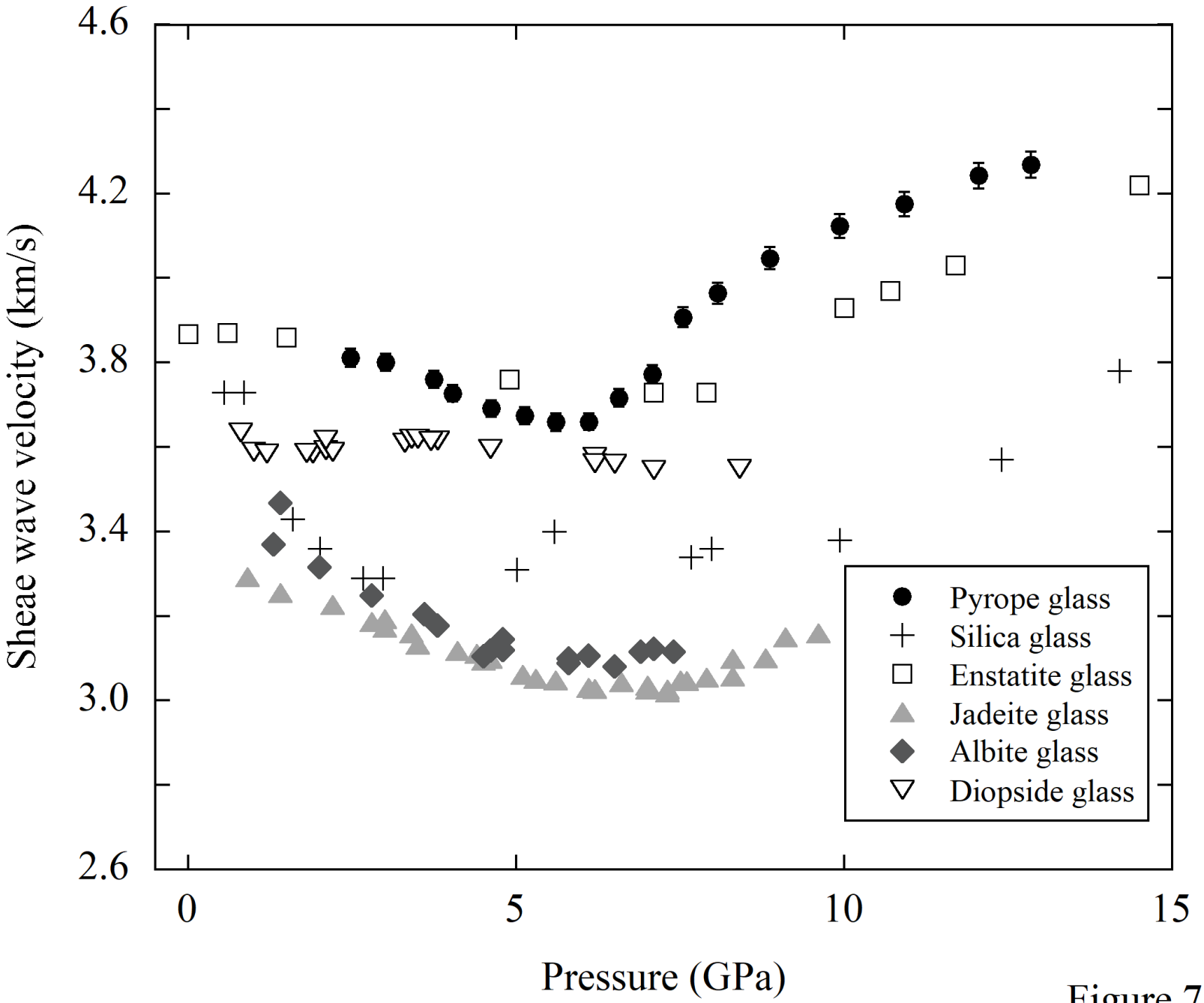
4.6
4.2
3.8
3.4
3.0
2.6
Sheae wave velocity (km/s)
0
5
10
15
Pressure (GPa)
Pyrope glass
Silica glass
Enstatite glass
Jadeite glass
Albite glass
Diopside glass

Figure 7

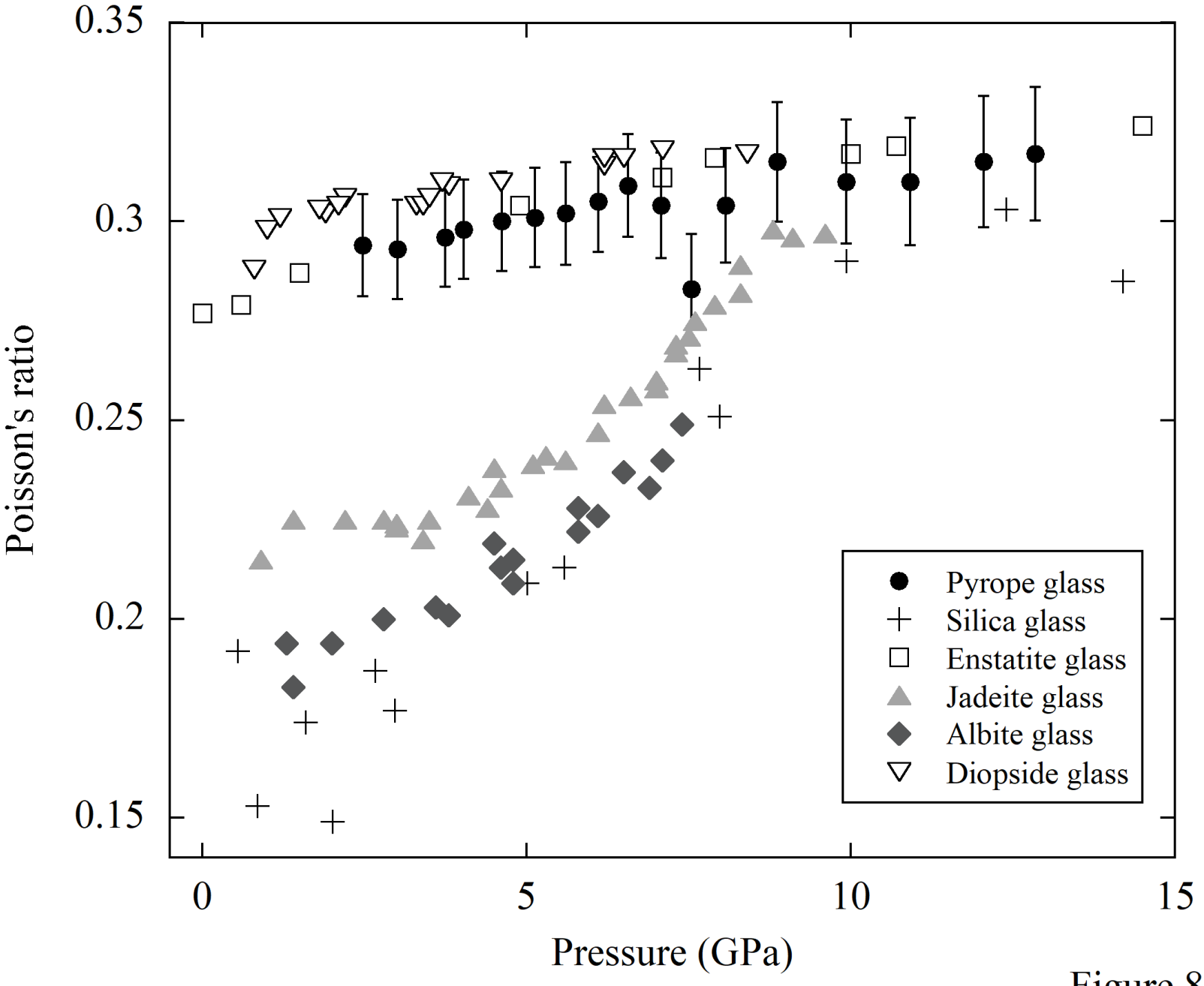
0.35
0.3
0.25
0.2
0.15
Poisson's ratio
0
5
10
15
Pressure (GPa)
Pyrope glass
Silica glass
Enstatite glass
Jadeite glass
Albite glass
Diopside glass

Figure 8